

Lateral migration of a deformable fluid particle in a square channel flow of viscoelastic fluid

Hafiz Usman Naseer¹, Daulet Izbassarov², Zaheer Ahmed³ and Metin Muradoglu^{1,†}

¹Department of Mechanical Engineering, Koç University, 34450 Istanbul, Türkiye

²Finnish Meteorological Institute, Erik Palménin aukio 1, 00560 Helsinki, Finland

³Department of Mechanical Engineering, SZAB Campus, Mehran University of Engineering and Technology, Khairpur Mirs, Pakistan

(Received 21 February 2024; revised 26 July 2024; accepted 28 July 2024)

Cross-stream migration of a deformable fluid particle is investigated computationally in a pressure-driven channel flow of a viscoelastic fluid via interface-resolved simulations. Flow equations are solved fully coupled with the Giesekus model equations using an Eulerian–Lagrangian method and extensive simulations are performed for a wide range of flow parameters to reveal the effects of particle deformability, fluid elasticity, shear thinning and fluid inertia on the particle migration dynamics. Migration rate of a deformable particle is found to be much higher than that of a solid particle under similar flow conditions mainly due to the free-slip condition on its surface. It is observed that the direction of particle migration can be altered by varying shear thinning of the ambient fluid. With a strong shear thinning, the particle migrates towards the wall while it migrates towards the channel centre in a purely elastic fluid without shear thinning. An onset of elastic flow instability is observed beyond a critical Weissenberg number, which in turn causes a path instability even for a nearly spherical particle. An inertial path instability is also observed once particle deformation exceeds a critical value. Shear thinning is found to be suppressing the path instability in a viscoelastic fluid with a high polymer concentration whereas it reverses its role and promotes path instability in a dilute polymer solution. It is found that migration of a deformable particle towards the wall induces a secondary flow with a velocity that is approximately an order of magnitude higher than the one induced by a solid particle under similar flow conditions.

Key words: bubble dynamics, gas/liquid flow, viscoelasticity

† Email address for correspondence: mmuradoglu@ku.edu.tr

1. Introduction

Cross-stream or lateral migration of particles in a pressure-driven flow has been an active area of research due to its relevance in many industrial (Shannon *et al.* 2008; Vidic *et al.* 2013) and biological (Nagrath *et al.* 2007) applications. The phenomenon of lateral migration is specifically used for the manipulation of biological cells and particles in various microfluidic applications (Xuan, Zhu & Church 2010; Amini, Lee & Di Carlo 2014). The wall-normal component of force acting on the particle is responsible for its lateral migration and it is usually called the lift force. The lift force which is often relatively small in magnitude plays a central role in determining the final position of an individual particle and the particle distribution in particulate flows (Hidman *et al.* 2022).

The lateral motion of a particle was first investigated experimentally by Segre & Silberberg (1961) in a tube flow. Their observation was later confirmed by many experimental (Karnis & Mason 1966; Matas, Morris & Guazzelli 2004*b*) and numerical (Feng, Hu & Joseph 1994; Yang *et al.* 2005) studies. The same observation was made in rectangular channels where particles move towards or away from the channel wall in the cross-streamwise direction (Frank *et al.* 2003; Del Giudice *et al.* 2013; Wang, Yu & Lin 2018; Yuan *et al.* 2018). The situation becomes more involved when the ambient fluid is viscoelastic as the fluid elasticity plays its role in pushing the particle towards the centre of the channel (Seo, Kang & Lee 2014). In the case of viscoelastic fluids, most of the existing literature is primarily focused on solid particles suspended in a viscoelastic fluid (Villone *et al.* 2013). In the absence of inertia, the cross-stream migration of a non-deformable particle is not possible to occur in a confined Newtonian fluid flow due to the inherent reversibility of Stokes flow. However, the nonlinear characteristics of viscoelasticity provide the required irreversibility making the lateral migration possible in a complex fluid even with negligible inertia. The lateral migration of particles in complex fluids and their application in manipulating the particles in various microfluidic devices have been summarized in the review paper by D'Avino, Greco & Maffettone (2017).

In the presence of both inertia and viscoelasticity, several factors determine the orientation of particle migration in a pressure-driven channel flow. Some of these factors reported in numerous studies so far include shear-induced lift force (Saffman 1965), wall-induced lift force (Shi *et al.* 2020), fluid elasticity (Karnis & Mason 1966; Raffiee, Dabiri & Ardekani 2017), initial position of the particle (e.g. Villone *et al.* 2011), geometry of the channel (Yu *et al.* 2019), the shear thinning of the ambient fluid (Li, McKinley & Ardekani 2015) and particle rotation rate (the Magnus effect). The effects of one or more of these factors determine the migration of a particle towards or away from the channel wall. Moreover, the deformability of an object adds further complexity to this phenomenon, and therefore, the complex dynamics of lateral migration of deformable particles in viscoelastic fluids is yet to be fully explored. As a result of this migration, some interesting secondary flow features also emerge in the vicinity of the particle. One of them is a secondary flow which is perpendicular to the primary flow (streamwise) direction and may have a velocity as large as the order of the particle migration velocity. However, this secondary flow is generated in non-circular channels only by the viscoelastic fluids having a non-zero second normal stress difference (Debbaut *et al.* 1997).

When a spherical particle moves with a relative velocity in a shear flow, a force is exerted on the particle by the surrounding fluid in a direction perpendicular to its relative motion. This force is known as the shear-induced lift force, first calculated analytically by Saffman (1965) for a solid sphere. This force pushes the particle towards the channel wall until it is balanced by the wall-induced lift force (Feng *et al.* 1994; Matas, Morris & Guazzelli 2004*a*). The flow field around the particle is significantly influenced by the

presence of the wall. The wall decelerates the motion of the particle in the streamwise direction due to extra drag and repels it away from the wall if the characteristic length of the particle is much smaller than the channel size. If the characteristic length of the particle is comparable to the channel size, like the motion of bubbles in capillaries, the channel walls constrain the motion of the immersed object, as explained by Michaelides (2006).

The well-known Magnus effect (rotation-induced lift force) is another factor influencing the migration of an object in the channel flow. For a solid particle having the no-slip condition on its surface, the difference in the relative fluid velocity on its sides may cause it to rotate. This shear-induced rotation generates an additional transverse pressure difference and the resulting lift force is referred to as the ‘Magnus effect’ (Rubinow & Keller 1961). Instead of a solid particle, if the object is deformable, the deformability induces yet another lateral migration directed towards the channel centre (Chan & Leal 1979). Similarly, the initial position of the particle in the channel has a direct impact on its lateral migration as dictated by the gradient of velocity at that initial location. The size of the particle as compared with the channel is another important variable to be considered while analysing the lateral migration in a pressure-driven flow. It is generally characterized by the blockage ratio (Di Carlo 2009) defined as $b = d/H$, where d is the particle size (e.g. diameter) and H is the channel width. It has been observed in both experimental (Lim *et al.* 2014) and numerical (Mortazavi & Tryggvason 2000) works that a deformable object with a diameter beyond a certain limit migrates towards the channel centre due to deformation-induced lift force while a smaller one migrates towards the wall due to inertial lift force. This feature is used in many microfluidic devices for sorting particles of different sizes (Nam *et al.* 2015).

The Magnus effect, shear-induced lift force and wall-induced lift force may be referred to as the ‘inertial effects’ as all these forces primarily originate due to fluid inertia. If the ambient fluid is viscoelastic, the elastic effects tend to push the object towards the centre (Seo *et al.* 2014) while the inertial effects tend to move it towards the channel wall. The relative strength of inertia and elasticity determines the final equilibrium position of a non-deformable particle in a channel. This interplay between inertia and elasticity is quantified by the elasticity number, defined as $El = Wi/Re$, where Wi and Re are the Weissenberg number and the Reynolds number, respectively. Furthermore, if the ambient fluid exhibits a shear-thinning behaviour as well, it has been reported by Li *et al.* (2015) that the shear thinning amplifies inertial effects and thus promotes particle migration towards the wall. Hazra, Mitra & Sen (2020) experimentally studied the role of shear thinning on the cross-stream migration of droplets in a confined shear flow for $Re < 1$. They observed that larger droplets followed their original streamlines while the smaller ones migrated towards the centre. Similarly, to predict the role of elasticity, Mukherjee & Sarkar (2014) performed computational simulations of a viscoelastic drop in a Newtonian fluid for a linear shear flow with negligible inertia. They found a non-monotonic impact of elasticity on the migration velocity of the droplet.

The above-mentioned list of factors affecting the migration dynamics of a deformable object is still not exhaustive. In the presence of surfactant contamination, the surfactant-induced Marangoni stresses oppose the inertial lift force and can completely alter the migration dynamics of an object. In our earlier work (Muradoglu & Tryggvason 2014; Ahmed *et al.* 2020b), it was observed that, in the pressure-driven channel flow of a Newtonian fluid, clean spherical bubbles move towards the wall while the deformable ones migrate away from it. However, even the spherical bubbles can move away from the wall in the presence of a strong enough surfactant.

Although there are a large number of experimental and numerical works devoted to solid particle migration, much less attention has been paid to the combined effects of inertia, viscoelasticity, and shear thinning on the lateral migration of a deformable fluid particle and only a few details are available in the existing literature, which motivates the present study. The main focus here is to explore the combined effects of fluid inertia, viscoelasticity and particle deformability on its lateral migration in a shear-thinning viscoelastic fluid. For this purpose, fully interface-resolved numerical simulations are performed using an Eulerian–Lagrangian method (Tryggvason *et al.* 2001) for a wide range of relevant flow parameters to explore the features of this complex flow field. In addition to the lateral migration, the particle-induced elastic instability and its impact on the onset of a path instability, the effect of shear thinning, and the resulting flow are investigated computationally. The secondary flow field developed due to the second normal stress difference in the flow is also examined and quantified.

The rest of the paper is organized as follows. The problem statement and the computational set-up are described in the next section. The governing equations and the numerical method are briefly described in § 3. The results are presented and discussed in § 4 followed by the conclusions in § 5. A grid convergence study is conducted and the results are presented in the Appendix.

2. Problem statement and computational set-up

Microfluidic devices usually use channels with rectangular cross-sections due to their relative ease of fabrication. If the aspect ratio of the channel is reduced, the relative influence of channel walls on the flow field becomes more pronounced (Villone *et al.* 2013). The limiting case is obtained for a square-shaped cross-section, which is selected in the present study. Figure 1(a) shows the computational domain which is a square channel with the dimensions of H , L and H in the x , y and z directions, respectively. Periodic boundary conditions are applied in the streamwise (y) direction whereas the other two directions (x and z) have no-slip/no-penetration boundary conditions. The centroid of the particle is denoted by (x_b, y_b, z_b) and a spherical fluid particle of diameter d is initially located at $(x_{bi}, y_{bi}, z_{bi}) = (0.5H, H, 0.25H)$ unless specified otherwise. The value of H is set to $4d$. After performing the simulations by gradually increasing the length of the channel in the streamwise (y) direction to check the effects of periodicity, the channel length is set to $L = 4H$, which is found to be sufficient to eliminate any significant effects of periodicity.

The deformable particle is at rest initially at $t = 0$ and a constant pressure gradient $dp_0/dy = -U_o\mu_o\pi^3/4kH^2$ is applied in the y -direction to drive the flow, where U_o is the flow velocity at the centreline of the channel in the case of a fully developed single-phase laminar flow and k is a geometric constant. For a square channel, $k \approx 0.571$ (Fetecau & Fetecau 2005). It is important to note that U_o is the centreline velocity in the channel for the Newtonian and Oldroyd-B fluids. In a Giesekus fluid, the centreline velocity becomes greater than U_o due to the shear-thinning effect. However, throughout this paper, all the non-dimensional numbers are defined based on U_o corresponding to the applied pressure gradient in the Newtonian fluid unless stated otherwise. Here, H , U_o and H/U_o are used as the length, velocity and time scales, respectively. The stresses are normalized by $\mu_o U_o/H$. The normalized non-dimensional quantities are denoted by the superscript (*). The blockage ratio ($b = d/H$) is fixed at 0.25. The density (ρ_o/ρ_i) and the viscosity (μ_o/μ_i) ratios are set to 10 in this study where the subscripts i and o denote the dispersed and continuous phases, respectively. These comparatively smaller ratios are used to reduce the spatial error exacerbated by sudden jumps in material properties across the interface

Lateral migration of a deformable particle

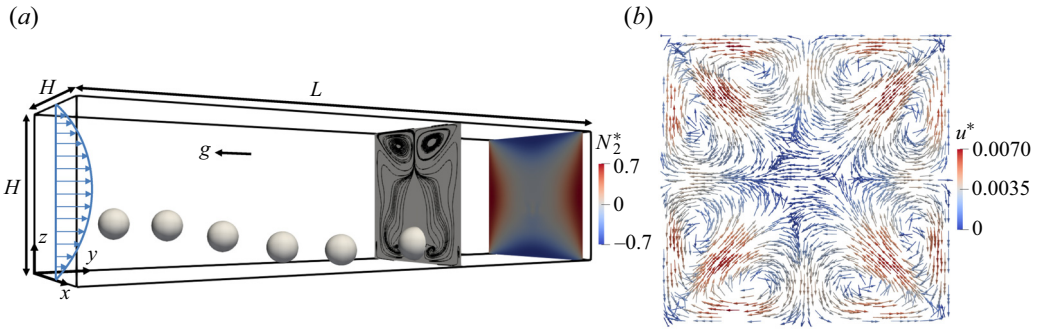


Figure 1. (a) Computational domain shown with the schematic representation of a deformable fluid particle migrating towards the wall of the channel. The streamlines of the flow are shown above the particle in the xz -plane once the particle reaches its equilibrium position closer to the wall. The distribution of the second normal stress difference (N_2^*) is shown in the xz -plane upstream of the particle at $y = 3.95$. (b) Eight vortices showing the secondary flow field in the same xz -plane away from the particle at $y = 3.95$ are shown. The velocity vectors are coloured by the magnitude of flow velocity in that plane. ($Re = 18.9$, $El = 0.05$, $Eo = 0$, $Ca = 0.01$, $\alpha = 0.1$.)

and enhance numerical stability, and thus relax the excessive grid resolution requirement and time step restrictions. Tasoglu *et al.* (2010) and Olgac, Izbassarov & Muradoglu (2013) have demonstrated that the results are not affected significantly for these types of flows at higher ratios. In the present case of pressure-driven viscoelastic channel flow, although not shown here, simulations have been performed for the density and viscosity ratios of 20, 40 and 80 as well, and the results are found to be not very sensitive to the increase in the density ratio, i.e. the difference is less than 1% but more sensitive to the viscosity ratio due to a higher contribution of polymeric viscosity in a concentrated polymer solution. It is observed that at a higher viscosity ratio, the secondary flow velocity induced by the fluid particle once it attains its equilibrium position (as will be discussed in detail in § 4.4) is not much affected but the lateral displacement of the fluid particle is still significantly influenced by this higher viscosity ratio. As the viscosity ratio in the liquid–air system of a complex fluid flow can be as high as 10^8 depending upon the molecular weight and concentration of the polymer molecules, the term ‘deformable fluid particle’ is used instead of a bubble in the present study.

In addition to the density and viscosity ratios, the flow conditions are characterized by the following non-dimensional numbers defined as

$$Re = \frac{\rho_o U_o H}{\mu_o}, \quad Wi = \frac{\lambda U_o}{H}, \quad Eo = \frac{g \Delta \rho d^2}{\sigma}, \quad Mo = \frac{g \mu_o^4}{\rho_o \sigma^3}, \quad Ca = \frac{\mu_o U_o}{\sigma}, \quad \beta = \frac{\mu_s}{\mu_o}, \quad (2.1a-f)$$

where Re , Wi , Eo , Mo and Ca denote the Reynolds, Weissenberg, Eötvös, Morton and capillary numbers, respectively. Note that the Morton number is not an independent parameter. Additionally, β is the ratio of solvent viscosity to zero shear viscosity of the viscoelastic fluid. The density difference is defined as $\Delta \rho = \rho_o - \rho_i$. The particle deformation (χ) is quantified as

$$\chi = \sqrt{I_{max}/I_{min}}, \quad (2.2)$$

where I_{max} and I_{min} are the maximum and minimum eigenvalues of the second moment of inertia tensor defined as

$$I_{ij} = \frac{1}{V_b} \int_V (x_i - x_{io})(x_j - x_{jo}) dV, \quad (2.3)$$

where \mathcal{V}_b is the volume of the particle, and x_{i0} and x_{j0} are the coordinates of the particle centroid in the i th and j th directions, respectively. Bunner & Tryggvason (2003) have shown that deformation quantified by this method is approximately equal to the ratio of the shortest to the longest axis for modestly deformed ellipsoids. However, for complex particle shapes, this definition of deformation gives a more general measure for the particle deformation and eliminates uncertainty in identifying the longest and the shortest axes.

3. Governing equations and numerical method

The flow and the Giesekus model equations are described here in the context of the Eulerian–Lagrangian method that uses a one-field formulation. As discussed by Tryggvason, Scardovelli & Zaleski (2011), Ahmed *et al.* (2020a), Izbassarov *et al.* (2021) and Izbassarov & Muradoglu (2015), one set of governing equations can be written for the entire multiphase computational domain. In this approach, the effect of surface tension is taken into account by adding a distributed body force term to the momentum equations near the interface, and the discontinuities in material properties are handled by defining an indicator function. The Navier–Stokes equations are thus written as

$$\rho \frac{\partial \mathbf{u}}{\partial t} + \rho \nabla \cdot (\mathbf{u}\mathbf{u}) = -\nabla p - \frac{dp_0}{dy} \mathbf{j} + \nabla \cdot \boldsymbol{\tau} + \nabla \cdot \mu_s (\nabla \mathbf{u} + \nabla \mathbf{u}^T) + \mathbf{g} (\rho - \rho_{ave}) + \int_A \sigma \kappa \mathbf{n} \delta(\mathbf{x} - \mathbf{x}_f) dA, \tag{3.1}$$

where \mathbf{u} , $\boldsymbol{\tau}$, p , ρ , μ_s are the velocity vector, polymer stress tensor, pressure, discontinuous density and solvent viscosity fields, respectively. A constant pressure gradient $-(dp_0/dy)\mathbf{j}$ is applied to drive the flow where \mathbf{j} is the unit vector in the y -direction. The buoyancy term consists of the gravitational acceleration \mathbf{g} and the density difference $\rho - \rho_{ave}$, where ρ_{ave} is the average density in the computational domain. The effect of surface tension is added as a body force term on the right-hand side of the momentum equation where σ is the surface tension coefficient, κ is twice the mean curvature and \mathbf{n} is a unit vector normal to the interface. As the surface tension acts only on the interface, δ represents a three-dimensional Dirac delta function with the arguments \mathbf{x} and \mathbf{x}_f being a point at which the equation is evaluated and a point at the interface, respectively. The momentum equation is supplemented by the continuity equation

$$\nabla \cdot \mathbf{u} = 0. \tag{3.2}$$

It is assumed that the material properties remain constant following a fluid particle, i.e.

$$\frac{D\rho}{Dt} = 0, \quad \frac{D\mu_s}{Dt} = 0, \quad \frac{D\mu_p}{Dt} = 0, \quad \frac{D\lambda}{Dt} = 0, \tag{3.3a-d}$$

where $D/Dt = \partial/\partial t + \mathbf{u} \cdot \nabla$ is the material derivative. For a viscoelastic fluid, μ_p is the polymeric viscosity and λ is the polymer relaxation time.

Using an indicator function (I), the material properties are set in the entire computational domain as

$$\left. \begin{aligned} \rho &= \rho_o I(\mathbf{x}, t) + \rho_i (1 - I(\mathbf{x}, t)), \\ \mu_s &= \mu_{s,o} I(\mathbf{x}, t) + \mu_{s,i} (1 - I(\mathbf{x}, t)), \\ \mu_p &= \mu_{p,o} I(\mathbf{x}, t) + \mu_{p,i} (1 - I(\mathbf{x}, t)), \\ \lambda &= \lambda_o I(\mathbf{x}, t) + \lambda_i (1 - I(\mathbf{x}, t)), \end{aligned} \right\} \tag{3.4}$$

where the subscripts ‘*i*’ and ‘*o*’ denote the properties of the particle and the bulk fluid, respectively. Since the fluid in the dispersed phase is Newtonian, the values of $\mu_{p,i}$ and λ_i are set to zero. The indicator function is defined as

$$I(\mathbf{x}, t) = \begin{cases} 1, & \text{in the bulk fluid,} \\ 0, & \text{in the particle.} \end{cases} \quad (3.5)$$

Viscoelasticity of bulk liquid is modelled using the Giesekus model (Giesekus 1982). This model is capable of capturing the elongation of individual polymer chains and the resulting shear-thinning behaviour of the viscoelastic fluid. In the Giesekus model, the polymer stress tensor $\boldsymbol{\tau}$ evolves by

$$\boldsymbol{\tau} = \frac{\mu_p}{\lambda} (\mathbf{B} - \mathbf{I}), \quad (3.6)$$

where \mathbf{B} and \mathbf{I} are the conformation and the identity tensors, respectively. The conformation tensor evolves by

$$\frac{\partial \mathbf{B}}{\partial t} + \mathbf{u} \cdot \nabla \mathbf{B} - \nabla \mathbf{u}^T \cdot \mathbf{B} - \mathbf{B} \cdot \nabla \mathbf{u} = \frac{1}{\lambda} \left[(1 - \alpha) \mathbf{I} + (2\alpha - 1) \mathbf{B} - \alpha \mathbf{B}^2 \right], \quad (3.7)$$

where α is the mobility factor representing the anisotropy of the hydrodynamic drag exerted on the polymer molecules. Due to the thermodynamic considerations, α is restricted to $0 \leq \alpha \leq 0.5$ (Schleiniger & Weinacht 1991). When $\alpha = 0$, the Giesekus model reduces to the Oldroyd-B model.

At high Weissenberg numbers, these highly nonlinear viscoelastic constitutive equations become extremely stiff, which makes their numerical solution a challenging task. The problem is overcome by using the well-known log-conformation method where an eigen decomposition is employed to re-write the constitutive equation of the conformation tensor in terms of its logarithm (Izbassarov & Muradoglu 2015; Izbassarov *et al.* 2018). The interested readers are referred to Fattal & Kupferman (2005) for the detailed procedure.

The flow equations (3.1) and (3.2) are solved fully coupled with the Giesekus model equation (3.6). The momentum, continuity and viscoelastic constitutive equations are solved on a stationary staggered Eulerian grid. A QUICK scheme is used to discretize the convective terms in the momentum equations while second-order central differences are used for the diffusive terms. For the convective terms in the viscoelastic equations, a fifth-order WENO-Z scheme (Borges, Carmona & Costa 2008) is used. A fast Fourier transform (FFT)-based solver is used for the pressure Poisson equation. Since the pressure equation is not separable due to variable density in the present multiphase flow, the FFT-based solvers cannot be used directly. To overcome this challenge, a pressure-splitting technique presented by Dong & Shen (2012) and Dodd & Ferrante (2014) is employed. The fluid–fluid interface is tracked by using the Lagrangian marker points located at the vertices of a triangular surface mesh. The marker points move with the local flow velocity interpolated from the Eulerian grid. The surface tension is computed on the Lagrangian grid and transferred to the Eulerian grid to be added to the momentum equation as a body force in a conservative manner. The Lagrangian grid is restructured at every time step to keep the surface mesh nearly uniform, smooth and comparable to the Eulerian grid. The indicator function is computed based on the location of the interface using the standard procedure as described by Tryggvason *et al.* (2011), which requires a solution of a separable Poisson equation. The same FFT-based solver is used to compute the indicator function. Once the indicator function is computed, the material properties are set in each phase using (3.4), which results in a smooth transition of material properties across the

interface. A predictor-corrector scheme is used to achieve second-order time accuracy as described by Tryggvason *et al.* (2001). The details of this Eulerian–Lagrangian method can be found in the book by Tryggvason *et al.* (2011) and in the review paper by Tryggvason *et al.* (2001), and the treatment of the viscoelastic model equations in Izbassarov & Muradoglu (2015) and Izbassarov *et al.* (2018).

4. Results and discussions

We first examine the dynamics of a nearly spherical fluid particle under similar conditions as used by Li *et al.* (2015) for a solid particle, i.e. $Re = 18.9$, $El = 0.05$, $Ca = 0.01$, $\alpha = 0$. The main difference in the present case is the slip at the particle interface. Note that this set of parameters is also designated as the baseline case in the present study to facilitate direct comparison with the results obtained for a solid particle by Li *et al.* (2015).

A peculiar feature of a viscoelastic fluid flow is the presence of normal stress differences, which are given by $N_1 = \tau_{yy} - \tau_{zz}$ and $N_2 = \tau_{zz} - \tau_{xx}$ in the present scenario. In the absence of the shear-thinning effect ($\alpha = 0$), the Giesekus model reduces to the Oldroyd-B model and the second normal stress difference (N_2) becomes zero. Thus, $\alpha > 0$ is an essential condition to model a viscoelastic fluid that exhibits a non-zero second normal stress difference. The geometry of the channel also plays a significant role in the development of these stresses. Here, N_1 is found to be maximum in the highest shear region near the walls, and its value becomes minimum in the corners and at the centre. Ho & Leal (1976) argued that this particular distribution of N_1 in a four-wall channel is the primary reason for the accumulation of solid particles in the corner and centreline regions. When the second normal stress difference develops in a shear-thinning viscoelastic fluid, not only does the distribution of N_1 in the channel change, but its magnitude is also reduced due to enhanced inertial effects (Li *et al.* 2015). Figure 1(a) shows the distribution of N_2 in the channel cross-section when there is a strong shear-thinning effect present in the flow, i.e. $\alpha = 0.1$. Eight vortices generated due to this distribution of N_2 away from the particle are also depicted in figure 1(b). This particular distribution of N_2 affects the orientation of particle migration and the development of a secondary flow field around the particle. An asymmetric pattern of streamlines is shown in figure 1(a) above the particle once the particle reaches its equilibrium position near the wall. These effects on the lateral migration of a deformable particle are explored one by one in the subsequent sections.

4.1. Dynamics of particle migration

Simulations are first performed to examine the effects of the Weissenberg number, the capillary number, the initial position and the mobility factor on the lateral migration of a non-buoyant particle in the channel flow at the nominal Reynolds number $Re = 18.9$ and $\beta = 0.1$. Figures 2(a) and 2(b) show the evolution of particle displacement in the lateral (z) direction and the corresponding change in the particle deformation during its migration, respectively. In a Newtonian fluid, a nearly spherical particle slightly moves towards the channel wall under the effects of inertia and stabilizes near the wall where wall-induced repulsive force balances the lift force. When the ambient fluid is viscoelastic, modelled by Oldroyd-B ($\alpha = 0$), the same spherical particle moves towards the centre of the channel under the elastic effects just like a solid particle (Li *et al.* 2015). It is observed that although the overall trend of fluid particle displacement in the Oldroyd-B fluid is similar to that of a solid particle, the fluid particle moves towards the centre of the channel at a much higher rate as shown in figure 2(c). Compared with a solid particle, a fluid particle experiences a smaller drag due to slip at the interface, which makes it more sensitive

to the inertial and elastic effects. When the particle deformability is increased gradually by increasing the capillary number to $Ca = 0.05$ and $Ca = 0.1$ for the same Oldroyd-B fluid, the rate of particle migration towards the channel centre is slightly reduced. As the particle moves towards the low shear region (towards the centre), its deformability starts to reduce and the same effect is observed in its lateral velocity as well. The effects on particle velocity will be discussed in detail later in § 4.5. It is interesting to observe that, although the deformability-induced lift force is expected to push the particle towards the centre, it acts in the opposite direction at this Reynolds number and slows down the particle migration towards the centre of the channel. Evolution of streamwise and wall normal velocities of the spherical and the slightly deformable particle are shown in figure 3, where the constant contours of viscoelastic stress components of τ_{yz} and τ_{zz} are also plotted in the insets in the yz -cutting plane. As seen, not only the wall-normal velocity but also the streamwise velocity is reduced when the particle is made slightly deformed by increasing the capillary number to $Ca = 0.1$, although the deformation is still modest, i.e. $\chi \approx 1.05$. The viscoelastic stress distribution is also markedly different in both cases. This extreme sensitivity is attributed to a similar mechanism that is responsible for a jump discontinuity in the rise velocity of a buoyancy-driven bubble (Bothe *et al.* 2022). A different manifestation of the same mechanism has also been observed in our earlier work (Naseer *et al.* 2023) as well. According to the theory proposed by Bothe *et al.* (2022), polymer molecules are stretched by the flow as they pass over the particle and this stored elastic energy is released on its front/back hemisphere giving an additional pull/push to the particle depending on the flow conditions. The transition is expected to occur when the convective time scale is equal to the polymer relaxation time, i.e. the effective Weissenberg number is unity. In the present scenario, the effective Weissenberg number can be defined as $Wi_{eff} = \lambda/(R/u_{rel})$, where R is the particle radius and u_{rel} is the slip velocity. For the nearly spherical particle, the effective Weissenberg number is computed as $Wi_{eff} = 0.92$ at $t^* = 5.53$ which is close to the critical value of unity. As the particle is elongated in the streamwise direction in the deformable case, the effective radius (minor axis) becomes larger so the polymer molecules relax on the front part of the particle before reaching the equator, which thus increases the drag and slows down the particle migration velocity.

When the shear-thinning effects are enhanced by increasing the mobility parameter (α) in the Giesekus model, the orientation of particle migration changes due to an increase in the relative importance of the fluid inertia. At a very small value of $\alpha = 0.01$, a spherical particle still moves towards the centre but it takes a comparatively longer time than that in the Oldroyd-B fluid to reach its equilibrium position. Once α is increased further to 0.1, the orientation of particle migration changes completely, i.e. instead of moving towards the centre, it starts moving towards the wall. Again, although the trend is similar to that of a solid particle in a shear-thinning fluid under the same parametric settings, the migration of a fluid particle is significantly more sensitive to the shear-thinning parameter than the corresponding solid particle. For example, while $\alpha = 0.2$ is required by the solid particle to reverse its orientation from the channel centre towards the wall (Li *et al.* 2015), $\alpha = 0.1$ is sufficient for the fluid particle to reverse its orientation. The shear-thinning effect is quantified by the reduction in the effective viscosity (μ_e) of the fluid defined as

$$\mu_e/\mu_o = \frac{\mu_s \left(\frac{\partial v}{\partial z} + \frac{\partial w}{\partial y} \right) + \tau_{yz}}{\mu_o \left(\frac{\partial v}{\partial z} + \frac{\partial w}{\partial y} \right)}. \tag{4.1}$$

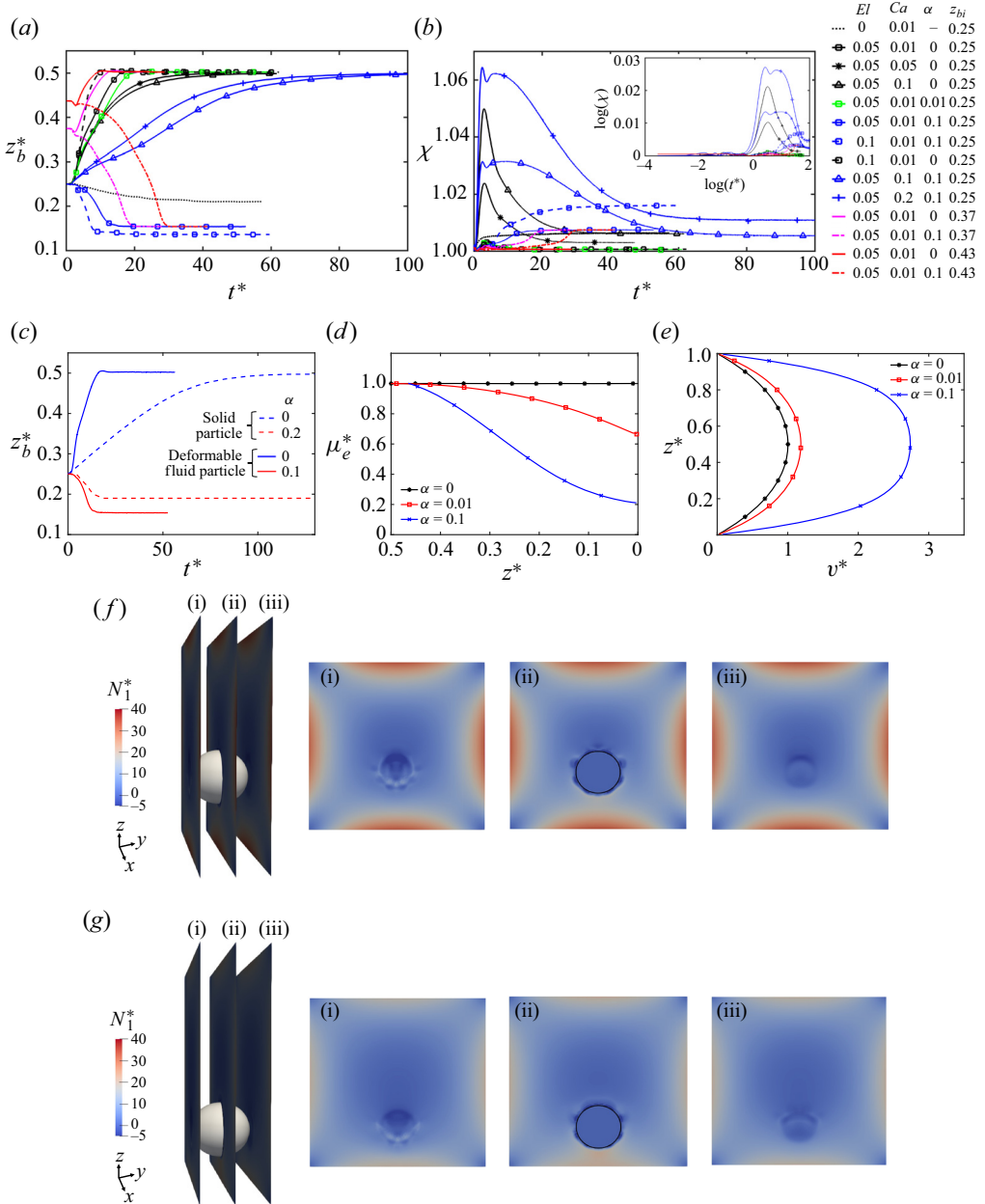


Figure 2. (a) Evolution of fluid particle displacement in the wall-normal (z) direction under non-buoyant conditions for different initial positions and flow conditions. (b) Corresponding change in the particle deformation shown as the particle moves towards or away from the wall. The same plot is shown in the inset on a log-scale. (c) Evolution of the fluid particle displacement compared with a solid particle studied by Li *et al.* (2015) under similar flow conditions. (d) Reduction in the effective viscosity of the fluid due to shear thinning quantified in a vertical cutting xz -plane away from the particle. (e) Flow velocity profiles in the same xz -plane shown for different values of α . The distributions of the first normal stress difference (N_1) around the particle are shown in vertical cutting planes of (i), (ii) and (iii) as indicated on the left for (f) $\alpha = 0.01$ and for (g) $\alpha = 0.1$. For panels (c–g), $El = 0.05$, $Ca = 0.01$. Additionally, $Re = 18.9$ for all the cases presented in this figure.

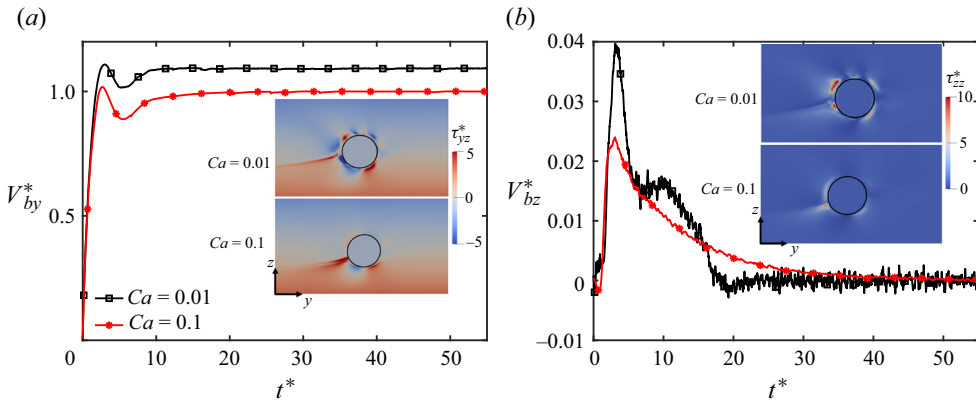


Figure 3. Evolution of migration velocity of a nearly spherical ($Ca = 0.01$) and a slightly deformed ($Ca = 0.1$) fluid particle (a) in the streamwise and (b) in the wall-normal directions. The contours of viscoelastic stress components τ_{yz} and τ_{zz} are shown in the insets around the particles in the yz -cutting plane at $t^* = 5.53$ ($Re = 18.9$, $El = 0.05$, $\alpha = 0$).

The variation of the effective viscosity and the corresponding flow velocity profiles are shown in figures 2(d) and 2(e), respectively, for $\alpha = 0, 0.01$ and 0.1 . As seen, for $\alpha = 0$, the effective viscosity remains constant in the channel as expected. In a shear-thinning fluid ($\alpha > 0$), the viscosity of the fluid decreases significantly in the high shear region near the wall and becomes as low as 20 % of its value in the channel centre for $\alpha = 0.1$. As a result, the centreline flow velocity becomes approximately 2.8 times larger than that of the non-shear-thinning fluid (figure 2e). This enhanced inertia helps the quick migration of the particle towards the wall as seen in figure 2(a). It is observed that this shear-thinning effect is strong enough to reverse the migration of fluid particle from the centre towards the wall even when the initial position of the particle is shifted gradually towards the channel centre, i.e. a low shear region (figure 2a). The shear thinning also changes the distribution of the first normal stress difference (N_1) in the channel. The distribution of N_1 is shown in three vertical cutting planes in the vicinity of the particle for $\alpha = 0.01$ and $\alpha = 0.1$ in figures 2(f) and 2(g), respectively, at the same time instant $t^* = 5.71$. The higher magnitude of N_1 for $\alpha = 0.01$ explains why the particle is pushed towards the channel centre. It is important to note that in the present study, as the channel aspect ratio is fixed (square duct only) and the initial position of the fluid particle is varied along one wall-normal direction (z) only while the initial position of the particle is fixed at $x = 0.5H$ in the second wall-normal direction, the equilibrium positions of the fluid particle along the channel diagonals or in the corner regions are not observed (Yu *et al.* 2019).

When the elasticity number is increased to $El = 0.1$ by increasing the Weissenberg number in the presence of a strong shear-thinning effect ($\alpha = 0.1$) for a spherical particle ($Ca = 0.01$), the viscoelastic stresses take more time to develop due to a higher relaxation time (λ) of polymer molecules. Therefore, the enhanced inertia due to the shear thinning quickly moves the particle towards the wall while the viscoelastic stresses are not yet fully developed in the flow. The particle reaches its equilibrium position closer to the wall and its deformation also increases due to a higher shear region there. However, this higher deformability and higher elasticity are not strong enough to reverse the particle migration back towards the channel centre. In the absence of the shear thinning ($\alpha = 0$) with the same high elasticity number, the particle quickly moves towards the centre due to relatively lower inertia.

When the fluid particle is made more deformable by increasing the capillary number to $Ca = 0.1$ (figure 2*b*) in this shear-thinning fluid ($\alpha = 0.1$), the deformability-induced lift force resists the pronounced effects of shear thinning on the fluid inertia. This higher particle deformation is sufficient enough to push the particle back towards the channel centre. However, due to the resistance by the higher inertial force, the rate of particle migration is much slower in this fluid than in the non-shear-thinning fluid. When the capillary number is increased even further to $Ca = 0.2$, the effect is found to be more pronounced and the rate of particle migration towards the centre of the channel is slightly increased. The enhanced fluid inertia due to the shear-thinning effect also makes the particle more deformable in a shear-thinning fluid due to an effective high capillary number.

For all the simulations shown in figure 2, the nominal Reynolds number is kept constant. It can be observed that in this non-buoyant situation, the orientation of particle migration can be controlled with the shear-thinning effect of the viscoelastic fluid. With a strong shear-thinning effect ($\alpha = 0.1$), the particle moves towards the wall and higher elasticity (e.g. $El = 0.1$) is not able to reverse its orientation. The higher particle deformability, however, resists this shear-thinning effect on particle migration and moves it back towards the centre. Interestingly, the particle deformation increases only by 6% in the case of the maximum capillary number of $Ca = 0.2$ in this viscoelastic fluid. However, even this modest deformation makes a significant impact on the dynamics of particle migration and reverses its orientation towards the centre. In the absence of shear thinning, the particle migrates towards the centre even with a weak elastic effect or with a little deformability.

4.2. Path instability

Path instability of a freely rising bubble in a Newtonian fluid has been thoroughly studied and well documented in the existing literature. For instance, Zenit & Magnaudet (2008) experimentally observed that the path instability of a bubble does not depend on the Reynolds number and it is rather governed by the aspect ratio of bubble shape, i.e. its deformation. When the aspect ratio increases beyond $\chi > 2$, vortices generated on the free-slip surface of the bubble give rise to a wake instability behind the trailing edge, forcing its path to become unstable. In the case of a viscoelastic ambient fluid, Shew & Pinton (2006) observed that the flow structure in the wake region becomes more intense leading to path instability even at a much lower deformability.

Simulations are first performed for $Re = 100, 500$ and 1000 to examine the effects of the Reynolds number on the path instability of the deformable fluid particle in the present pressure-driven viscoelastic flow in the absence of buoyancy. To isolate the effects of the Reynolds number, the shear-thinning effect is eliminated by setting $\alpha = 0$, and the capillary number is fixed at $Ca = 0.01$ to keep the particle nearly spherical. Simulations are repeated by keeping either the elasticity number or the Weissenberg number constant as the Reynolds number is increased. The results are summarized in figures 4(*a,c*) and 4(*b,d*) for the fixed elasticity number and the fixed Weissenberg number cases, respectively. When the elasticity number is kept constant at $El = 0.05$ (figure 4*a*), the Weissenberg number increases as the Reynolds number is increased. The particle path becomes unstable at $Re = 100$ (the corresponding $Wi = 5$). However, the particle deformation remains negligible due to a low value of the capillary number. The path instability observed in this case of a nearly spherical particle at $Re = 100$ occurs mainly due to the onset of an elastic flow instability caused by the curved streamlines along the particle interface. McKinley, Pakdel & Öztekin (1996) determined a critical parameter for the onset of an

Lateral migration of a deformable particle

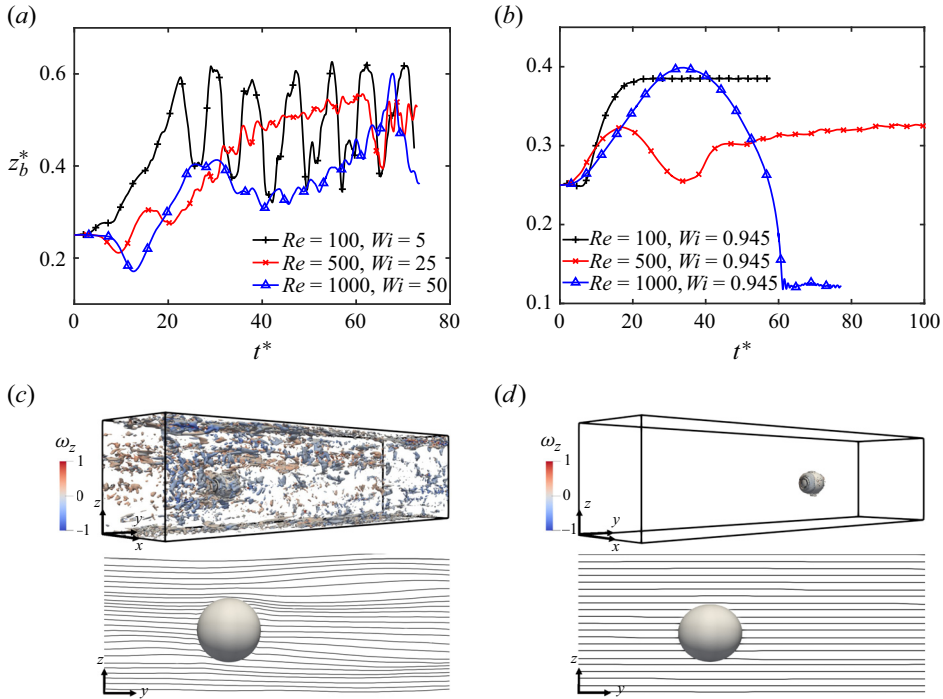


Figure 4. Evolution of lateral migration of the fluid particle (a) at constant $El = 0.05$ and (b) at constant $Wi = 0.945$ are shown for different values of Reynolds number. (c) Constant contours of Q-criterion at 0.001 coloured by the vorticity component (ω_z) shown for $Re = 500, Wi = 25$ as the flow becomes elastically unstable due to the curvature of streamlines across the particle. (d) Contours of Q-criterion plotted at the same value of 0.001 for $Re = 500, Wi = 0.945$ showing a negligible presence, confirming a stable flow. This is also confirmed by the straight streamlines across the fluid particle.

elastic instability as

$$M^2 = \frac{\lambda U N_1}{R |\tau_t|} \geq M_{crit}^2, \quad (4.2)$$

where U is the flow velocity along the streamline, N_1 is the first normal stress difference, R is the radius of curvature of the streamline and τ_t is the total shear stress. McKinley *et al.* (1996) calculated the critical value for a two-dimensional cylinder as $M_{crit} \approx 6.08$. In the present scenario of a spherical fluid particle, the critical value turns out to be $M_{crit} \approx 5.59$ at $Re = 100$. The constant contours of the Q-criterion (second invariant of velocity gradient tensor) at 0.001 and the streamlines are also plotted around the particle in figure 4(c) for $Re = 500$ to show the overall flow structure. The contours are coloured by the magnitude of vorticity in the z -direction. The curvature of streamlines across the particle and the contours of the Q-criterion confirm that the flow is no longer stable. As a result, the particle path shows an oscillatory pattern around the channel centre for $Re = 100$. When the Weissenberg number is increased further by increasing the Reynolds number at the fixed value of $El = 0.05$, figure 4(a) shows that the particle path becomes more irregular and unpredictable as the flow gets closer to the onset of elastic turbulence stemming from the elastic instability. The exact mechanism behind this probable transition is still elusive (Datta *et al.* 2022).

However, when the Weissenberg number is kept constant at $Wi = 0.945$ as Re is increased, the particle path remains stable even for the Reynolds number as high as

$Re = 1000$. As shown in figure 4(d), the streamlines remain straight across the particle and no significant contours of Q-criterion are observed in the flow, unlike the fixed elasticity number case. It is interesting to observe that the particle initially moves towards the channel centreline and then reverses its direction towards the channel wall at higher Reynolds numbers. The final position is determined by the interplay of inertial and viscoelastic effects. The equilibrium position of the particle shifts from the channel centre towards the wall as the Reynolds number is increased (figure 4b). At $Re = 1000$, the particle reaches the wall under the influence of strong inertia, which results in an increase in its deformation as well due to the high-shear region near the wall.

4.3. Effect of buoyancy

The buoyancy is significant in many natural processes and practical applications. A commonly encountered situation is an upward flow where the gravity acts in the opposite direction of the fluid flow such as in bubble column reactors and in crude oil extraction. Simulations are next performed for a range of Eötvös numbers to examine the effects of buoyancy in an upward flow while keeping the other parameters fixed at their baseline values of $Re = 18.9$, $Ca = 0.01$ and $El = 0.05$. Note that the Morton number is $M = 4.97 \times 10^{-6}$ for $Eo = 1$ in this viscoelastic fluid. For reference, this value is much higher than the Morton number of 2.52×10^{-11} for an air particle in water at 20°C but can be matched by using a water–glycerin solution (Legendre, Zenit & Velez-Cordero 2012).

Simulations are performed by gradually increasing the Eötvös number from $Eo = 0$ (neutrally buoyant) to $Eo = 1$ without and with the shear-thinning effect. The case of $Eo = 0$ is simulated by setting $g = 0$, which can be realistic only in a microgravity environment. This condition is used here to isolate the sole effects of the other parameters from buoyancy. The results are shown in figures 5(a,c,e,g) and 5(b,d,f,h) in terms of the evolution of particle deformation, its three-dimensional displacement, the wake structure behind the particle, and the pressure distribution on the particle surface for an Oldroyd-B ($\alpha = 0$) and a Giesekus ($\alpha = 0.1$) fluid case, respectively. In the Oldroyd-B fluid, the particle moves towards the channel wall without any sign of path instability at $Eo = 0.25$. We note that the same particle moves towards the channel centre in the absence of buoyancy. This change in the orientation occurs due to the additional buoyancy-induced lift force (Lu, Biswas & Tryggvason 2006). At $Eo = 0.5$, the particle still migrates towards a channel wall (interestingly not to the same wall as in the $Eo = 0.25$ case) but small oscillations start to appear in its path with a regular zigzag pattern indicating the onset of a path instability. A similar oscillatory pattern is also visible in the particle deformation (χ) as seen in figure 5(a). When Eo is further increased to 0.75, the particle deformation also increases and the particle path shifts from a zigzag to a helical pattern. The particle moves laterally to eventually settle near the other side of the channel and its motion becomes more chaotic with a significant velocity component in the wall normal (x) direction. At $Eo = 1$, the particle path becomes completely unstable with a deformation parameter (χ) exceeding 1.6 (figure 5a).

It is worth noting that the deformation parameter is only approximately $\chi = 1.1$ when the deformed particle undergoes path instability at $Eo = 0.5$ in the present setting. This value is much smaller than the condition $\chi \geq 2$ required for the onset of a path instability in the case of a freely rising bubble in a Newtonian fluid (Zenit & Magnaudet 2008). This result confirms that the viscoelasticity facilitates the earlier onset of path instability as also pointed out by Shew & Pinton (2006). The wake region is much more intense in the viscoelastic fluid than in the Newtonian fluid due to the additional viscoelastic stresses, forcing its path to become unstable at a relatively small deformation. The evolution of

Lateral migration of a deformable particle

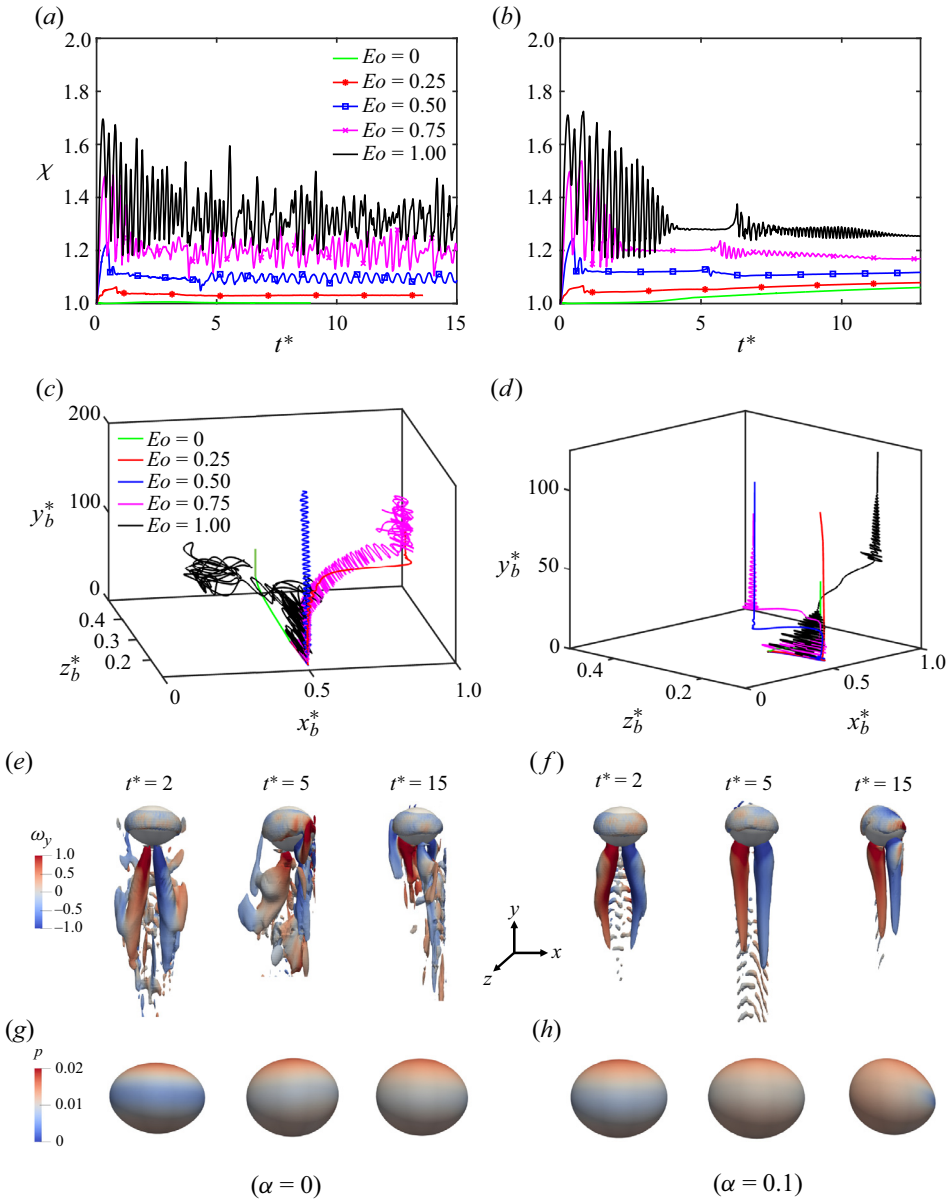


Figure 5. Evolution of particle deformation and its three-dimensional (3-D) displacement at different values of Eötvös number are shown for (a,c) $\alpha = 0$ and for (b,d) $\alpha = 0.1$. For the $Eo = 1$ case, the constant contours of the Q criterion at 0.05 are shown to visualize the complex flow pattern in the wake region for (e) $\alpha = 0$ and for (f) $\alpha = 0.1$. The contours are coloured by vorticity (ω_y) in the range of ± 1 . For the same $Eo = 1$ case, the pressure distribution on the particle surface are shown at the same times for (g) $\alpha = 0$ and for (h) $\alpha = 0.1$. ($Re = 18.9$, $Ca = 0.01$, $El = 0.05$, $\beta = 0.1$.)

the wake region and the corresponding pressure distribution on the particle surface is depicted for the $Eo = 1$ case in figures 5(e) and 5(g), respectively, to qualitatively show the mechanism for the path instability. As seen, the structure of the wake is highly complex and transient, and the pressure distribution changes accordingly, indicating the footprint of the instability.

Next, a strong shear-thinning effect is added ($\alpha = 0.1$), and the simulations are repeated for the same values of EO by keeping the other parameters fixed at their baseline values of $Re = 18.9$, $El = 0.05$ and $Ca = 0.01$. The results are summarized on the right-hand side of figure 5. As seen in figure 5(d), the particle migrates towards a wall for all the cases but interestingly not to the same wall. The path of the fluid particle remains stable for $EO = 0.25$ but it migrates towards the wall at a much higher rate than that for the non-buoyant case of $EO = 0$. This behaviour is attributed to the same enhanced lift force due to the buoyancy as in the non-shear-thinning case. Some oscillations appear in the particle trajectory for $EO = 0.5$ but they are damped very quickly as the particle stabilizes near a wall. As EO is increased beyond $EO = 0.5$, the oscillations are amplified leading to path instability. For $EO = 0.75$, the particle migrates laterally and settles near the other wall similar to the Oldroyd-B fluid case. In this case, the particle initially follows a helical path but, interestingly, its path is stabilized after some time (figure 5d). The corresponding oscillatory pattern observed in the deformation also vanishes once the particle path is stabilized (figure 5b). The stabilized particle path is also observed for $EO = 1$. The stabilization mechanism is visualized in figure 5(f) where the evolution of the wake structure is depicted for the $EO = 1$ case. As seen, the wake behind the particle is not symmetric initially but it later evolves into a symmetric two counter-rotating vortex structures indicating that the path is stabilized. Two contributory factors are speculated to be the main reason for this stabilization mechanism. First, with a decrease in fluid viscosity in the vicinity of the particle due to the shear-thinning effect, the vortices generated on the surface of the deformed particle are not strong enough to make the wake region unstable. Second, due to the shear thinning of the fluid, the first normal stress difference N_1 decreases in this viscoelastic fluid, which reduces the destabilization effect of viscoelasticity. Thus, the intense flow structures observed in the wake region in the case of the Oldroyd-B fluid (figure 5e) are damped out in this shear-thinning fluid (figure 5f). Although an addition of shear thinning makes the particle path more stable, it cannot maintain path stability indefinitely. For instance, although not shown here due to space consideration, once the particle deformation exceeds $\chi > 2$ at $EO = 2$, the path remains unstable even for the mobility factor as high as $\alpha = 0.1$.

All the simulations have heretofore been performed for a small value of the viscosity ratio, $\beta = 0.1$, representing highly concentrated polymer solutions. Thus, the fluid exhibited a strong viscoelastic behaviour and the particle path remained stable only up to $EO = 0.25$ and $EO = 1$ without and with the shear-thinning effect, respectively. To examine the particle migration dynamics in dilute polymer solutions, simulations are now performed for another extreme value of $\beta = 0.9$ without and with the shear-thinning effect. It is important to note that $\beta = 0.9$ represents a very rare case that can be achieved only with specially designed fluids. Figure 6(a,b) show the evolution of lateral displacement of a particle and its deformation for the range of $2 \leq EO \leq 8$. We note that at the lower values of EO up to $EO = 2$, there is not much difference observed in the particle deformation and its equilibrium position compared with the case of $EO = 2$ in figure 6(a). As EO increases, the difference in the equilibrium position of the particle becomes increasingly more pronounced without and with the shear-thinning effect. For the smaller values of Eötvös number up to $EO = 2$, the shear-thinning effect does not play a dominant role due to a lower value of particle deformation. As the contribution of polymeric viscosity towards the total viscosity of the fluid is already very low at $\beta = 0.9$, a further decrease in the viscosity due to shear thinning starts to show its effect only at a higher value of particle deformation. Beyond $EO = 2$ and with $\alpha = 0.1$, the particle reaches the channel centre for all the values of EO up to $EO = 8$, whereas without the shear-thinning effect, the equilibrium position of the particles occurs slightly away from the centre depending

Lateral migration of a deformable particle

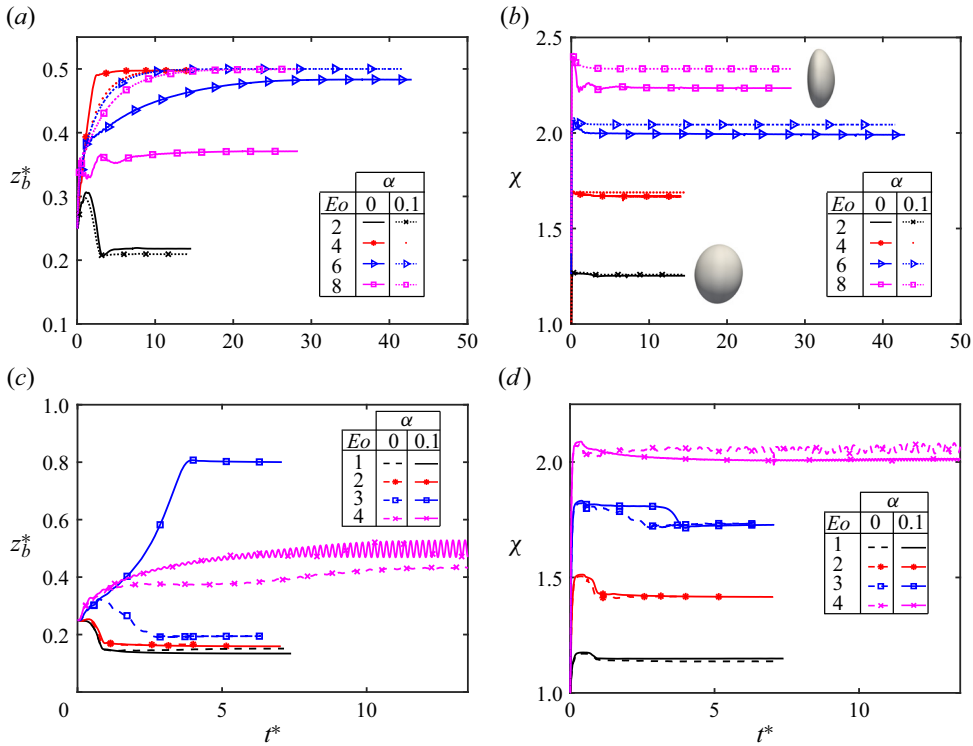


Figure 6. (a) Evolution of particle displacement in the lateral (z) direction and (b) its deformation for different values of Eötvös number. For panels (a,b), $Re = 18.9$, $Ca = 0.01$, $El = 0.05$, $\beta = 0.9$. For panels (c,d), $Re = 47.25$, $Ca = 0.01$, $El = 0.02$, $\beta = 0.9$. The shapes of the deformed fluid particles are shown in the inset of panel (b) for $\alpha = 0$ case at $Eo = 2$ and $Eo = 8$.

upon its deformation. The most interesting feature is the persistent stability of the particle path even when the deformation exceeds 2.3 for the $Eo = 8$ case (figure 6b inset). Zenit & Magnaudet (2008) have shown that for a freely rising bubble, the path becomes unstable when the deformation value exceeds 2. They argued that for such a buoyancy-driven bubble, path instability depends upon the bubble deformation rather than the Reynolds number. However, Haberman & Morton (1953) and Kelley & Wu (1997) had earlier demonstrated that the path instability of an air bubble in a viscous fluid of a Hele-Shaw cell did depend on the Reynolds number. It is found that the criterion, $\chi > 2$, for triggering path instability does not apply in the present case of a pressure-driven viscoelastic channel flow at this low Reynolds number.

To verify the dependence of path instability of the fluid particle on the Reynolds number, simulations are next performed by increasing the Reynolds number to 47.25 while keeping the Weissenberg number fixed at $Wi = 0.945$. As a result, the elasticity number is reduced to 0.02. Simulations are repeated for $\alpha = 0$ (no shear thinning) and $\alpha = 0.1$ (significant shear thinning) cases for the range of Eötvös number $1 \leq Eo \leq 4$. Figure 6(c,d) depict the evolution of particle displacement in the lateral direction and its deformation. As Eo increases, the particle deformation also increases and its equilibrium position gradually shifts away from the wall. At $Eo = 3$, as the fluid viscosity decreases in the vicinity of the particle, the elastic effect becomes dominant and the particle migrates towards the channel centre. The particle crosses the channel centre under the combined effects of

deformation-induced lift force and the fluid elasticity, and settles at an equilibrium position closer to the wall on the other side of the channel as the inertial effects eventually dominate (figure 6c). However, without shear thinning, the particle migrates towards the wall as the deformation and elasticity are not strong enough to counter high inertial lift force at $Eo = 3$. Interestingly, both the particles settle at the same equilibrium position closer to the wall but on the opposite sides of the channel.

At $Eo = 4$, when the particle deformation exceeds 2 and the shear-thinning effect is present, small oscillations start to appear in its path indicating the onset of a path instability. It shows that path instability of the fluid particle in this pressure-driven viscoelastic flow is a function of Reynolds number as well along with the particle deformation. It is also observed that the particle path remains stable in the absence of shear thinning ($\alpha = 0$) at the same value of $Eo = 4$. Interestingly, this role of shear thinning is opposite to what was observed in the case of $\beta = 0.1$, i.e. the shear thinning damps out the path instability at low values of β (high polymer concentration) whereas it promotes the path instability of the particle at high β values (dilute polymer concentration). This interesting behaviour is attributed to the local change in the effective elasticity number (El) due to the shear-thinning effect. Ray & Zaki (2014) have shown that, for larger values of El , there is an asymptotic limit of stabilization observed in the Oldroyd-B model. We find that this role of elasticity number in stabilizing or destabilizing the particle path is further dependent upon the value of β . At lower β , a decrease in the local value of El stabilizes the particle path while, at the higher value of β , the same decrease in El is found to be destabilizing.

4.4. Particle-induced secondary flow

The presence of the second normal stress difference (N_2) and the geometry of the square-shaped channel induces a secondary flow field in a direction perpendicular to the primary flow. The dynamics of this secondary flow field is significantly influenced by the presence of a fluid particle. Moreover, the orientation of particle migration also affects the magnitude of the secondary flow velocity. The secondary flow velocity has been analysed by varying the particle deformability (Ca), the shear thinning (α), the fluid elasticity (Wi) and the fluid inertia (Re). Figure 7 shows complex flow patterns in vertical cutting planes at the downstream, the centre and upstream of the particle under different flow conditions. The upstream and downstream planes are located at $+0.75$ and -0.75 from the particle centre, respectively. The velocity vectors are coloured by the magnitude of flow velocity in the xz -plane. In an Oldroyd-B fluid, the particular distribution of N_1 in the channel far away from the particle builds up a weak secondary flow oriented towards the corners of the channel from its centre. It generates a ‘flower-shaped’ flow pattern as shown in figure 7(a). The presence of N_2 due to the shear-thinning effect (Giesekus fluid) generates an additional eight vortices at the corners of the channel (figure 7d). Once the particle passes through this plane and migrates towards the centre (figure 7g,h), this flow pattern gets disturbed but becomes symmetric again above and below the particle once the particle attains its steady-state position. However, if the particle migrates towards a channel wall, the flow pattern becomes highly asymmetric away from the wall resulting in a strong secondary flow with a velocity as high as the order of particle migration velocity (figure 7k).

The quantitative comparison of secondary flow velocities is summarized in figure 8 for different flow conditions. The z -component of flow velocity is numerically integrated in the region ± 0.75 upstream and downstream of the particle in the streamwise (y) direction

Lateral migration of a deformable particle

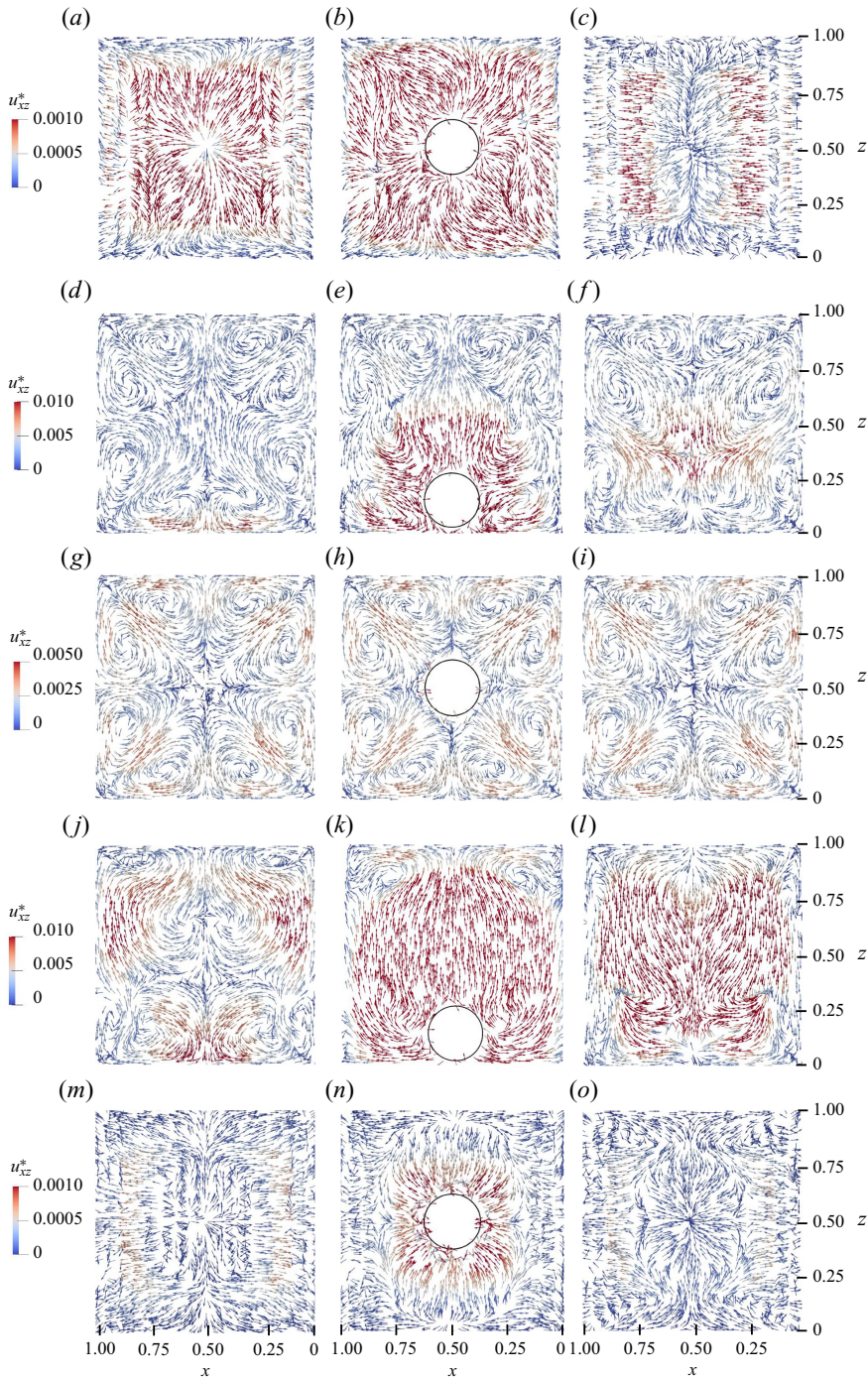


Figure 7. Velocity vectors representing the complex flow patterns of secondary flow field in vertical cutting planes at (a,d,g,j,m) a downstream, (b,e,h,k,n) the centre and (c,f,i,l,o) upstream of the particle. (a-c) $Re = 18.9$, $Ca = 0.01$, $El = 0.05$, $\alpha = 0$. (d-f) $Re = 18.9$, $Ca = 0.01$, $El = 0.05$, $\alpha = 0.1$. (g-i) $Re = 18.9$, $Ca = 0.2$, $El = 0.05$, $\alpha = 0.1$. (j-l) $Re = 18.9$, $Ca = 0.01$, $El = 0.1$, $\alpha = 0.1$. (m-o) $Re = 18.9$, $Ca = 0.1$, $El = 0.05$, $\alpha = 0$.

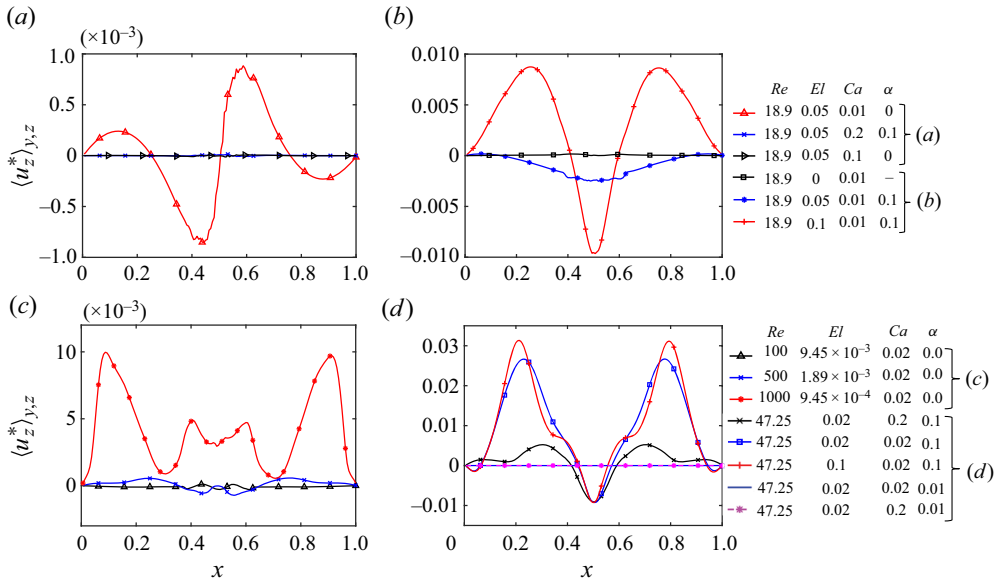


Figure 8. Averaged secondary flow velocity under the flow conditions (a) where the fluid particle migrates towards the channel centre and (b) where the particle migrates towards a wall at $Re = 18.9$. The averaged secondary flow velocity is plotted for higher Reynolds numbers in the range $47.25 \leq Re \leq 1000$ for (c) an Oldroyd-B fluid and (d) a Giesekus fluid.

and the integration is performed in the entire domain $[0, 1]$ in the z -direction, i.e.

$$\langle u_z \rangle_{y,z} = \frac{1}{A_{yz}} \int_0^1 \int_{-0.75}^{+0.75} u_z \, dz \, dy \cong \frac{1}{(j_{max} - j_{min} + 1) N_z} \sum_{k=1}^{N_z} \sum_{j=j_{min}}^{j_{max}} (u_z)_{jk}, \quad (4.3)$$

where A_{yz} is the area of the yz -plane, and $j_{min} = (y_b - 0.75)N_y/L$ and $j_{max} = (y_b + 0.75)N_y/L$ with N_y and N_z being the number of grid points in the y and z directions, respectively. The average secondary velocity, $\langle u_z \rangle_{y,z}$, in the y and z directions is plotted along x in figure 8 once the particle reaches its equilibrium position closer to a wall or towards the centre of the channel. Figure 8(a,b) show the average secondary flow velocity for $Re = 18.9$ while the results for higher Reynolds numbers are shown in figure 8(c,d).

At $Re = 18.9$, the magnitude of the secondary flow velocity remains negligible for all the situations where the particle migrates towards the channel centre (figure 8a). In an Oldroyd-B fluid, the particle migrates towards the centre of the channel under the effect of elasticity, as shown in figure 2. As the particle migrates in the z -direction and reaches the centre, the flow pattern becomes symmetric above and below the particle (figure 7b). In a Giesekus fluid, when the shear-thinning effect is sufficient enough to move the particle towards a wall ($\alpha = 0.1$), a strong secondary flow pattern is observed as shown in figure 8(b). When the elasticity number is increased in this shear-thinning fluid, the maximum magnitude of the secondary flow velocity is attained. This is the same combination of parameters for which the particle equilibrium position is closest to the channel wall in figure 2(a). The flow pattern above the particle for this situation is depicted in figure 7(k). When the Reynolds number is increased in an Oldroyd-B fluid, the equilibrium position of the particle moves closer to the channel wall. When the Weissenberg number is kept constant while increasing the Reynolds number to avoid elastic instability, as discussed in § 4.2, the magnitude of the secondary flow velocity keeps

increasing with the Reynolds number and becomes as high as 1 % of the maximum flow velocity in the channel (figure 8c). A small asymmetry observed in the secondary flow pattern for the $Re = 1000$ case is attributed to the slight migration of the particle in the x -direction due to onset of an inertial path instability.

At $Re = 47.25$, when the shear-thinning effect is small ($\alpha = 0.01$), the particle moves towards the centre of the channel whether it is spherical ($Ca = 0.01$) or highly deformable ($Ca = 0.1$). The secondary flow velocity remains negligible for both of these situations (figure 8d). However, this time, the magnitude of the secondary flow velocity depends on the particle deformability along with the fluid elasticity. When the particle deformability is increased, the magnitude of the secondary flow velocity is reduced whereas an increase in the fluid elasticity (Wi) further increases its magnitude. Thus, a nearly spherical particle migrating towards the channel wall induces maximum secondary flow due to the maximum asymmetric area of influence above. This area reduces with the particle deformability and hence a reduction in the induced secondary flow is observed. Similarly, a higher magnitude of viscoelastic stresses due to higher Wi generates a complex flow pattern in the direction normal to the primary flow. This flow pattern becomes increasingly more asymmetric with increasing Wi and as a result, the secondary flow velocity becomes as high as 3 % of the maximum flow velocity in this square channel (figure 8d).

It can be summarized that an increase in the fluid elasticity (Wi) or inertia (Re) increases the magnitude of the secondary flow velocity as long as the particle moves towards a wall. If the flow conditions are such that the particle moves towards the channel centre, an increase in the inertia or elasticity of the fluid makes negligible impact on the velocity of the secondary flow once the particle reaches its steady-state position. However, during the transient period while the particle is still migrating towards the centre, the inertia and fluid elasticity do make an impact on the velocity of the secondary flow but its magnitude during this transient period remains two orders of magnitude lower than the corresponding cases where the particle migrates towards the wall.

It is important to note that the secondary flow velocity induced by a fluid particle is at least an order of magnitude higher than the velocity induced by the solid particle under the similar flow conditions as reported by Li *et al.* (2015). The primary reason is the higher drag experienced by the solid particle due to the no-slip condition on its surface. This attribute of fluid particle-induced secondary flow can be exploited in the situations where mixing, heat transfer or other transport phenomena are of importance.

4.5. Flow start-up

It is a well-known aspect that stress waves propagate (Duarte, Miranda & Oliveira 2008) and cause velocity fluctuations during flow build-up in a channel flow. The elasticity of the fluid affects these fluctuations depending upon the relaxation time of its polymer molecules. In our earlier work (Naseer *et al.* 2023), these velocity fluctuations were also observed in the rise velocities of freely rising bubbles in a viscoelastic fluid. Similarly, these velocity fluctuations affect the migration velocity of the solid particle as well during the flow build-up (Rajagopalan, Arigo & McKinley 1996). Goyal & Derksen (2012) have shown that a solid particle settling down during these fluctuations often rebounds after the first oscillation. In the present study, we explore the same effects for a fluid particle in this viscoelastic channel flow.

Figure 9(a) shows the migration velocity of the particle in the wall-normal direction (z) under various flow conditions. The two cases are shown in the inset where the particle is highly deformable ($Ca = 0.1$ and $Ca = 0.2$) and it takes a comparatively longer time to reach a steady state. Figure 9(b) shows the evolution of the average streamwise component

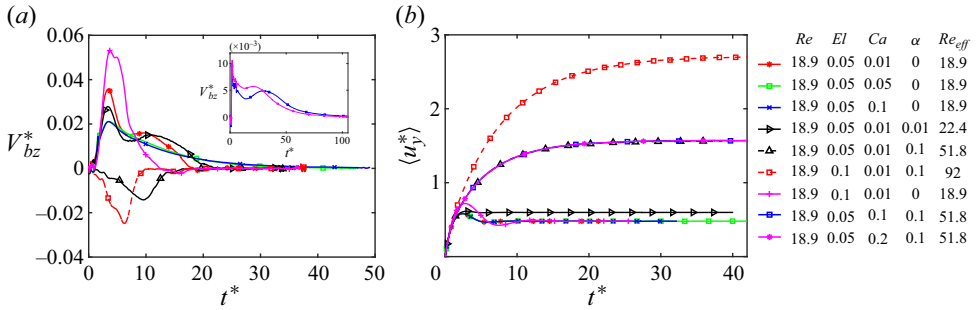


Figure 9. (a) Evolution of particle migration velocity in the wall-normal (z) direction during flow start-up. (b) Evolution of average streamwise component of flow velocity in the channel.

of flow velocity in the channel for the same nine situations. In the case of a nearly spherical particle (low Ca) migrating in an Oldroyd-B fluid ($\alpha = 0$), the elastic stresses develop quickly in the flow and take the particle towards the centre. As N_1 decreases in the low-shear region near the centre, the particle reaches its peak velocity at $t^* \approx 4$ and then starts to decelerate while continuing its migration towards the centre. The minor fluctuations in the particle velocity are attributed to the extension/relaxation of polymer molecules across its surface as recently explained by Bothe *et al.* (2022) and verified by Naseer *et al.* (2023). A minor decline in the flow velocity is observed after an initial peak once the viscoelastic stresses are developed in the flow (figure 9b). When the particle deformability is increased ($Ca = 0.05$ and $Ca = 0.1$), the particle starts migrating towards the channel centre. However, due to a slight increase in its deformability, the peak velocity of the particle migration remains lower than that of the nearly spherical particle. When a spherical particle ($Ca = 0.01$) migrates in the Giesekus fluid having a very low shear thinning ($\alpha = 0.01$), migration towards the channel centre occurs primarily due to the elastic effects and similar fluctuations are observed in the migration velocity as in the case of Oldroyd-B fluid. As the shear thinning promotes the relative importance of fluid inertia which acts to pull the particle back towards the wall, the peak velocity of the particle remains lower than that in the Oldroyd-B fluid. The average flow velocity is slightly increased in the channel due to the shear-thinning effect and the actual effective Reynolds number becomes $Re_{eff} = 22.4$. When the shear-thinning effect is high enough ($\alpha = 0.1$), the enhanced fluid inertia overcomes the elastic effects and causes the particle to migrate towards the wall, as indicated by the opposite direction of particle velocity in figure 9(a). The flow velocity in the channel increases further and the effective Reynolds number reaches 51.8 with the same value of an applied pressure gradient. When the elasticity number is increased ($El = 0.1$) by increasing the polymer relaxation time in this shear-thinning viscoelastic fluid, the inertial effects still dominate and push the particle towards a wall at a higher rate. With increased viscoelastic stresses at higher El and a strong shear-thinning effect, the effective Reynolds number reaches 92. With the same high elasticity number ($El = 0.1$) but without shear thinning ($\alpha = 0$), the particle migrates towards the centre under the elastic effects. Due to a higher Weissenberg number, the viscoelastic stresses become comparatively stronger and the particle reaches a higher value of its migration velocity. As there is no shear-thinning effect, the flow Reynolds number remains at the baseline value of $Re = 18.9$.

Once the particle is made highly deformable ($Ca = 0.1$ and $Ca = 0.2$) and the fluid is strongly shear thinning ($\alpha = 0.1$), the ‘deformability-induced’ lift force overcomes the

shear-thinning enhanced inertial effects and the particle moves towards the channel centre. As the particle gets closer to the centre, its deformability starts reducing due to low shear (as shown in [figure 2b](#)) resulting in a deceleration in its lateral migration velocity. It is worth noting that the effective flow Reynolds number becomes $Re_{eff} = 51.8$ due to a strong shear-thinning effect in this case.

5. Conclusions

Interface-resolved numerical simulations are performed to explore the complex dynamics of cross-stream migration of a fluid particle in a viscoelastic pressure-driven channel flow for a wide range of flow parameters. Unlike the solid particle, the deformability of the fluid particle, the slip condition at the interface and the particle-induced elastic flow instability at a higher Weissenberg number add further complexity to this phenomenon. The particle deformability (Ca), shear thinning of the ambient fluid (α), fluid elasticity (Wi), buoyancy (EO) and concentration of polymers (β) are varied one by one to isolate their sole effects. The conditions for triggering a path instability of a deformable particle in this pressure-driven viscoelastic flow are investigated and the particle-induced secondary flow is quantified.

It is observed that the forces induced by fluid inertia push the particle towards the wall while elasticity and deformability pull it towards the channel centre. This interplay between fluid inertia, elasticity and particle deformability determines the orientation of particle migration in the channel and its final equilibrium position. As shear thinning increases the relative importance of the fluid inertia, it is found to promote migration towards a wall. At a high Weissenberg number, elastic instability occurs due to the curvature of streamlines across the particle. When the Reynolds number is increased while keeping the Weissenberg number fixed at a low value, the particle path remains stable even for the Reynolds number as high as $Re = 1000$.

In the case of a high polymer concentration (e.g. $\beta = 0.1$), it is found that strong viscoelastic effects make the particle path unstable even when the particle is nearly spherical. This path instability occurs as the flow itself becomes elastically unstable at a higher value of Wi . In the absence of strong viscoelastic stresses (low Wi), the path of the particle becomes unstable when its deformation becomes high due to high EO . However, the shear thinning acts as a stabilizing factor and can make the particle path stable even for the particle deformation as large as $\chi = 2$. The stabilizing role of shear thinning is reversed at higher values of β . When the Reynolds number is small and $\beta = 0.9$, the particle path remains stable even for the Eötvös number as large as $EO = 8$ and its deformation exceeds $\chi > 2.3$. Thus, the path instability of a deformable particle in a viscoelastic pressure-driven channel flow can occur when the flow itself becomes elastically unstable at high Wi or when its deformation exceeds a threshold value under buoyant conditions. If the path instability is triggered by the later mechanism, i.e. when the particle deformation exceeds a critical value, the shear thinning suppresses the path instability at higher polymer concentration (lower β) while it reverses its role and promotes the path instability at lower polymer concentration (higher β). Furthermore, it is found that the threshold value of particle deformation to trigger path instability is a function of Reynolds number as well in this pressure-driven viscoelastic flow unlike the path instability of a freely rising bubble in a Newtonian flow (Zenit & Magnaudet 2008).

It is shown that the secondary flow velocity induced by a fluid particle migrating towards the wall is an order of magnitude higher than the one induced by a solid particle under similar flow conditions. This behaviour is attributed to the slip condition on the particle

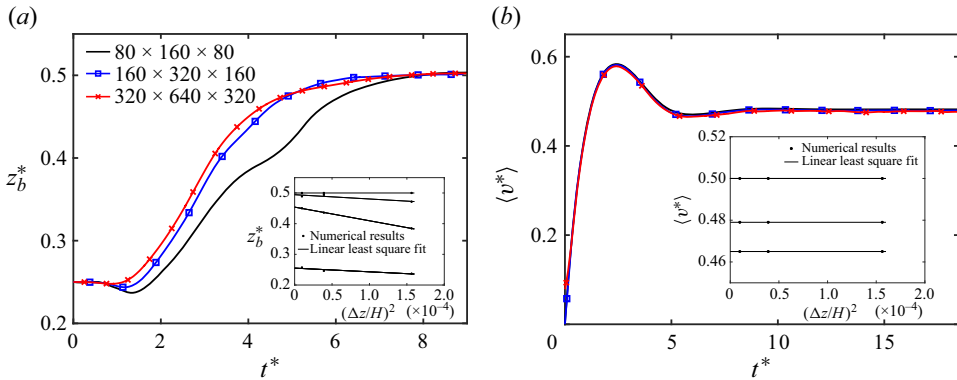


Figure 10. (a) Evolution of particle displacement in the wall-normal (z) direction and (b) the average streamwise component of flow velocity in the channel are shown at different grid resolutions. Linear least-squares fits at different time intervals are shown in the respective insets. ($Re = 18.9$, $El = 0.05$, $Ca = 0.01$, $\alpha = 0$).

surface and the internal flow. For all the situations where the fluid particle migrates towards the centre, the secondary flow velocity becomes negligible due to the symmetric flow pattern above and below the particle when viewed in its migrating plane.

During the flow build-up in this square-shaped channel, the maximum value of flow velocity depends upon the shear-thinning property of the fluid. The particle migration velocity is dictated by the inertial effects and the rate at which the viscoelastic stresses are built up in the flow.

Supplementary movie. A time-lapse movie showing the generation and growth of instabilities in the flow at a high Weissenberg number ($Re = 500$, $Wi = 25$) due to the presence of a deformable particle can be accessed at <https://doi.org/10.1017/jfm.2024.583>.

Funding. We acknowledge financial support from the Scientific and Technical Research Council of Turkey (TUBITAK; grant number 119M513) and the Research Council of Finland (grant number 354620).

Declaration of interests. The authors report no conflict of interest.

Data availability. Data can be made available upon request.

Author ORCIDs.

Hafiz Usman Naseer <https://orcid.org/0000-0001-6258-4038>;

Daultet Izbassarov <https://orcid.org/0000-0003-4791-3803>;

Metin Muradoglu <https://orcid.org/0000-0002-1758-5418>.

Appendix

A comprehensive grid convergence study is performed to ascertain the numerical accuracy of the results reported in this study. Figure 10(a) shows the evolution of particle displacement in the wall-normal (z) direction plotted at three different grid resolutions. Linear least-squares fits at $t^* = 1.38, 4, 6$ and 8 are shown in the inset of figure 10(a) where the approximately linear relations confirm the expected second-order spatial accuracy of the numerical scheme. These results show that a grid resolution containing $160 \times 320 \times 160$ grid cells in the $x, y,$ and z directions, respectively, is sufficient to reduce the spatial error below 3.5%. Therefore this grid resolution is used in all the simulations reported in this paper. Note that, for this grid resolution, there are about 40 grid points in the x

and z directions and 20 grid points in the streamwise (y) direction per particle diameter. Figure 10(b) shows the evolution of average flow velocity in the channel and the linear least-square fits shown in its inset confirm that the numerical error remains negligible for this quantity even with a grid size of $80 \times 160 \times 80$. The time step size is strictly restricted by the stability constraints in the present explicit numerical method and the temporal error remains negligible compared to the spatial error (Tryggvason *et al.* 2001, 2011). Therefore, a temporal error convergence is not examined.

REFERENCES

- AHMED, Z., IZBASSAROV, D., COSTA, P., MURADOGLU, M. & TAMMISOLA, O. 2020a Turbulent bubbly channel flows: effects of soluble surfactant and viscoelasticity. *Comput. Fluids* **212**, 104717.
- AHMED, Z., IZBASSAROV, D., LU, J., TRYGGVASON, G., MURADOGLU, M. & TAMMISOLA, O. 2020b Effects of soluble surfactant on lateral migration of a bubble in a pressure driven channel flow. *Intl J. Multiphase Flow* **126**, 103251.
- AMINI, H., LEE, W. & DI CARLO, D. 2014 Inertial microfluidic physics. *Lab on a Chip* **14** (15), 2739–2761.
- BORGES, R., CARMONA, M., COSTA, B. & DON, W.S. 2008 An improved weighted essentially non-oscillatory scheme for hyperbolic conservation laws. *J. Comput. Phys.* **227**, 3191–3211.
- BOTHE, D., NIETHAMMER, M., PILZ, C. & BRENN, G. 2022 On the molecular mechanism behind the bubble rise velocity jump discontinuity in viscoelastic liquids. *J. Non-Newtonian Fluid Mech.* **302**, 104748.
- BUNNER, B. & TRYGGVASON, G. 2003 Effect of bubble deformation on the properties of bubbly flows. *J. Fluid Mech.* **495**, 77–118.
- CHAN, P.-H. & LEAL, L. 1979 The motion of a deformable drop in a second-order fluid. *J. Fluid Mech.* **92** (1), 131–170.
- DATTA, S.S., *et al.* 2022 Perspectives on viscoelastic flow instabilities and elastic turbulence. *Phys. Rev. Fluids* **7** (8), 080701.
- D'AVINO, G., GRECO, F. & MAFFETTONE, P.L. 2017 Particle migration due to viscoelasticity of the suspending liquid and its relevance in microfluidic devices. *Annu. Rev. Fluid Mech.* **49**, 341–360.
- DEBBAUT, B., AVALOSSE, T., DOOLEY, J. & HUGHES, K. 1997 On the development of secondary motions in straight channels induced by the second normal stress difference: experiments and simulations. *J. Non-Newtonian Fluid Mech.* **69** (2–3), 255–271.
- DEL GIUDICE, F., ROMEO, G., D'AVINO, G., GRECO, F., NETTI, P.A. & MAFFETTONE, P.L. 2013 Particle alignment in a viscoelastic liquid flowing in a square-shaped microchannel. *Lab on a Chip* **13** (21), 4263–4271.
- DI CARLO, D. 2009 Inertial microfluidics. *Lab on a Chip* **9** (21), 3038–3046.
- DODD, M.S. & FERRANTE, A. 2014 A fast pressure-correction method for incompressible two-fluid flows. *J. Comput. Phys.* **273**, 416–434.
- DONG, S. & SHEN, J. 2012 A time-stepping scheme involving constant coefficient matrices for phase-field simulations of two-phase incompressible flows with large density ratios. *J. Comput. Phys.* **231** (17), 5788–5804.
- DUARTE, A.S.R., MIRANDA, A.I.P. & OLIVEIRA, P.J. 2008 Numerical and analytical modeling of unsteady viscoelastic flows: the start-up and pulsating test case problems. *J. Non-Newtonian Fluid Mech.* **154** (2–3), 153–169.
- FATTAL, R. & KUPFERMAN, R. 2005 Time-dependent simulation of viscoelastic flows at high weissenberg number using the log-conformation representation. *J. Non-Newtonian Fluid Mech.* **126** (1), 23–37.
- FENG, J., HU, H.H. & JOSEPH, D.D. 1994 Direct simulation of initial value problems for the motion of solid bodies in a Newtonian fluid. Part 2. Couette and Poiseuille flows. *J. Fluid Mech.* **277**, 271–301.
- FETECAU, C. & FETECAU, C. 2005 Unsteady flows of Oldroyd-B fluids in a channel of rectangular cross-section. *Intl J. Non-Linear Mech.* **40** (9), 1214–1219.
- FRANK, M., ANDERSON, D., WEEKS, E.R. & MORRIS, J.F. 2003 Particle migration in pressure-driven flow of a Brownian suspension. *J. Fluid Mech.* **493**, 363–378.
- GIESEKUS, H. 1982 A simple constitutive equation for polymer fluids based on the concept of deformation-dependent tensorial mobility. *J. Non-Newtonian Fluid Mech.* **11** (1–2), 69–109.
- GOYAL, N. & DERKSEN, J.J. 2012 Direct simulations of spherical particles sedimenting in viscoelastic fluids. *J. Non-Newtonian Fluid Mech.* **183**, 1–13.
- HABERMAN, W.L. & MORTON, R.K. 1953 *An Experimental Investigation of the Drag and Shape of Air Bubbles Rising in Various Liquids*. David W. Taylor Model Basin.

- HAZRA, S., MITRA, S.K. & SEN, A.K. 2020 Cross-stream migration of droplets in a confined shear-thinning viscoelastic flow: role of shear-thinning induced lift. *Phys. Fluids* **32** (9), 092007.
- HIDMAN, N., STRÖM, H., SASIC, S. & SARDINA, G. 2022 The lift force on deformable and freely moving bubbles in linear shear flows. *J. Fluid Mech.* **952**, A34.
- HO, B.P. & LEAL, L.G. 1976 Migration of rigid spheres in a two-dimensional unidirectional shear flow of a second-order fluid. *J. Fluid Mech.* **76** (4), 783–799.
- IZBASSAROV, D., AHMED, Z., COSTA, P., VUORINEN, V., TAMMISOLA, O. & MURADOGLU, M. 2021 Polymer drag reduction in surfactant-contaminated turbulent bubbly channel flows. *Phys. Rev. Fluids* **6** (10), 104302.
- IZBASSAROV, D. & MURADOGLU, M. 2015 A front-tracking method for computational modeling of viscoelastic two-phase flow systems. *J. Non-Newtonian Fluid Mech.* **223**, 122–140.
- IZBASSAROV, D., ROSTI, M.E., ARDEKANI, M.N., SARABIAN, M., HORMOZI, S., BRANDT, L. & TAMMISOLA, O. 2018 Computational modeling of multiphase viscoelastic and elastoviscoplastic flows. *Intl J. Numer. Meth. Fluids* **88** (12), 521–543.
- KARNIS, A. & MASON, S.G. 1966 Particle motions in sheared suspensions. XIX. Viscoelastic media. *Trans. Soc. Rheol.* **10** (2), 571–592.
- KELLEY, E. & WU, M. 1997 Path instabilities of rising air bubbles in a Hele-Shaw cell. *Phys. Rev. Lett.* **79** (7), 1265.
- LEGENDRE, D., ZENIT, R. & VELEZ-CORDERO, J.R. 2012 On the deformation of gas bubbles in liquids. *Phys. Fluids* **24** (4), 043303.
- LI, G., MCKINLEY, G.H. & ARDEKANI, A.M. 2015 Dynamics of particle migration in channel flow of viscoelastic fluids. *J. Fluid Mech.* **785**, 486–505.
- LIM, E.J., OBER, T.J., EDD, J.F., DESAI, S.P., NEAL, D., BONG, K.W., DOYLE, P.S., MCKINLEY, G.H. & TONER, M. 2014 Inertio-elastic focusing of bioparticles in microchannels at high throughput. *Nat. Commun.* **5** (1), 1–9.
- LU, J., BISWAS, S. & TRYGGVASON, G. 2006 A DNS study of laminar bubbly flows in a vertical channel. *Intl J. Multiphase Flow* **32** (6), 643–660.
- MATAS, J.-P., MORRIS, J.F. & GUAZZELLI, É. 2004b Inertial migration of rigid spherical particles in Poiseuille flow. *J. Fluid Mech.* **515**, 171–195.
- MATAS, J.P., MORRIS, J.F. & GUAZZELLI, E. 2004a Lateral forces on a sphere. *Oil Gas Sci. Technol.* **59** (1), 59–70.
- MCKINLEY, G.H., PAKDEL, P. & ÖZTEKIN, A. 1996 Rheological and geometric scaling of purely elastic flow instabilities. *J. Non-Newtonian Fluid Mech.* **67**, 19–47.
- MICHAELIDES, E. 2006 *Particles, Bubbles & Drops: Their Motion, Heat and Mass Transfer*. World Scientific.
- MORTAZAVI, S. & TRYGGVASON, G. 2000 A numerical study of the motion of drops in Poiseuille flow. Part 1. Lateral migration of one drop. *J. Fluid Mech.* **411**, 325–350.
- MUKHERJEE, S. & SARKAR, K. 2014 Lateral migration of a viscoelastic drop in a newtonian fluid in a shear flow near a wall. *Phys. Fluids* **26** (10), 103102.
- MURADOGLU, M. & TRYGGVASON, G. 2014 Simulations of soluble surfactants in 3D multiphase flow. *J. Comput. Phys.* **274**, 737–757.
- NAGRATH, S., *et al.* 2007 Isolation of rare circulating tumour cells in cancer patients by microchip technology. *Nature* **450** (7173), 1235–1239.
- NAM, J., NAMGUNG, B., LIM, C.T., BAE, J.-E., LEO, H.L., CHO, K.S. & KIM, S. 2015 Microfluidic device for sheathless particle focusing and separation using a viscoelastic fluid. *J. Chromatogr. A* **1406**, 244–250.
- NASEER, H.U., AHMED, Z., IZBASSAROV, D. & MURADOGLU, M. 2023 Dynamics and interactions of parallel bubbles rising in a viscoelastic fluid under buoyancy. *J. Non-Newtonian Fluid Mech.* **313**, 105000.
- OLGAC, U., IZBASSAROV, D. & MURADOGLU, M. 2013 Direct numerical simulation of an oscillating droplet in partial contact with a substrate. *Comput. Fluids* **77**, 152–158.
- RAFFIIE, A.H., DABIRI, S. & ARDEKANI, A.M. 2017 Elasto-inertial migration of deformable capsules in a microchannel. *Biomicrofluidics* **11** (6), 064113.
- RAJAGOPALAN, D., ARIGO, M.T. & MCKINLEY, G.H. 1996 The sedimentation of a sphere through an elastic fluid. Part 2. Transient motion. *J. Non-Newtonian Fluid Mech.* **65** (1), 17–46.
- RAY, P.K. & ZAKI, T.A. 2014 Absolute instability in viscoelastic mixing layers. *Phys. Fluids* **26** (1), 014103.
- RUBINOW, S.I. & KELLER, J.B. 1961 The transverse force on a spinning sphere moving in a viscous fluid. *J. Fluid Mech.* **11** (3), 447–459.
- SAFFMAN, P.G. 1965 The lift on a small sphere in a slow shear flow. *J. Fluid Mech.* **22** (2), 385–400.
- SCHLEINIGER, G. & WEINACHT, R.J. 1991 A remark on the Giesekus viscoelastic fluid. *J. Rheol.* **35** (6), 1157–1170.

Lateral migration of a deformable particle

- SEGRE, G. & SILBERBERG, A. 1961 Radial particle displacements in Poiseuille flow of suspensions. *Nature* **189**, 209–210.
- SEO, K.W., KANG, Y.J. & LEE, S.J. 2014 Lateral migration and focusing of microspheres in a microchannel flow of viscoelastic fluids. *Phys. Fluids* **26** (6), 063301.
- SHANNON, M.A., BOHN, P.W., ELIMELECH, M., GEORGIADIS, J.G., MARINAS, B.J. & MAYES, A.M. 2008 Science and technology for water purification in the coming decades. *Nature* **452** (7185), 301–310.
- SHEW, W.L. & PINTON, J.-F. 2006 Viscoelastic effects on the dynamics of a rising bubble. *J. Stat. Mech.* **2006** (01), P01009.
- SHI, P., RZEHAŁ, R., LUCAS, D. & MAGNAUDET, J. 2020 Hydrodynamic forces on a clean spherical bubble translating in a wall-bounded linear shear flow. *Phys. Rev. Fluids* **5**, 073601.
- TASOGLU, S., KAYNAK, G., SZERI, A.J., DEMIRCI, U. & MURADOGLU, M. 2010 Impact of a compound droplet on a flat surface: a model for single cell epitaxy. *Phys. Fluids* **22** (8), 082103.
- TRYGGVASON, G., BUNNER, B., ESMAEELI, A., JURIC, D., AL-RAWAHI, N., TAUBER, W., HAN, J., NAS, S. & JAN, Y.-J. 2001 A front-tracking method for the computations of multiphase flow. *J. Comput. Phys.* **169** (2), 708–759.
- TRYGGVASON, G., SCARDOVELLI, R. & ZALESKI, S. 2011 *Direct Numerical Simulations of Gas–Liquid Multiphase Flows*. Cambridge University Press.
- VIDIC, R.D., BRANTLEY, S.L., VANDENBOSSCHE, J.M., YOXTHEIMER, D. & ABAD, J.D. 2013 Impact of shale gas development on regional water quality. *Science* **340** (6134), 1235009.
- VILLONE, M.M., D’AVINO, G., HULSEN, M.A., GRECO, F. & MAFFETTONE, P.L. 2011 Simulations of viscoelasticity-induced focusing of particles in pressure-driven micro-slit flow. *J. Non-Newtonian Fluid Mech.* **166** (23–24), 1396–1405.
- VILLONE, M.M., D’AVINO, G., HULSEN, M.A., GRECO, F. & MAFFETTONE, P.L. 2013 Particle motion in square channel flow of a viscoelastic liquid: migration vs secondary flows. *J. Non-Newtonian Fluid Mech.* **195**, 1–8.
- WANG, P., YU, Z. & LIN, J. 2018 Numerical simulations of particle migration in rectangular channel flow of Giesekus viscoelastic fluids. *J. Non-Newtonian Fluid Mech.* **262**, 142–148.
- XUAN, X., ZHU, J. & CHURCH, C. 2010 Particle focusing in microfluidic devices. *Microfluid. Nanofluid.* **9**, 1–16.
- YANG, B.H., WANG, J., JOSEPH, D.D., HU, H.H., PAN, T.-W. & GLOWINSKI, R. 2005 Migration of a sphere in tube flow. *J. Fluid Mech.* **540**, 109–131.
- YU, Z., WANG, P., LIN, J. & HU, H.H. 2019 Equilibrium positions of the elasto-inertial particle migration in rectangular channel flow of Oldroyd-B viscoelastic fluids. *J. Fluid Mech.* **868**, 316–340.
- YUAN, D., ZHAO, Q., YAN, S., TANG, S.-Y., ALICI, G., ZHANG, J. & LI, W. 2018 Recent progress of particle migration in viscoelastic fluids. *Lab on a Chip* **18** (4), 551–567.
- ZENIT, R. & MAGNAUDET, J. 2008 Path instability of rising spheroidal air bubbles: a shape-controlled process. *Phys. Fluids* **20** (6), 061702.